

## Introducing the MISR Level 2 Near Real-Time Aerosol Product

Marcin. L. Witek<sup>1</sup>, Michael J. Garay<sup>1</sup>, David J. Diner<sup>1</sup>, Michael A. Bull<sup>1</sup>, Felix C. Seidel<sup>1</sup>, Abigail M. Nastan<sup>1</sup>, and Earl G. Hansen<sup>1</sup>

<sup>1</sup>Jet Propulsion Laboratory, California Institute of Technology, 4800 Oak Grove Drive, Pasadena, CA 91109, USA

### Abstract

Atmospheric aerosols are an important element of Earth's climate system, and have significant impacts on the environment and on human health. Global aerosol modeling has been increasingly used for operational forecasting and as support to decision making. For example, aerosol analyses and forecasts are routinely used to provide air quality information and alerts in both civilian and military applications. The growing demand for operational aerosol forecasting calls for additional observational data that can be assimilated into models to improve model accuracy and predictive skill. These factors have motivated the development, testing, and release of a new near real-time (NRT) level 2 (L2) aerosol product from the Multi-angle Imaging SpectroRadiometer (MISR) instrument on NASA's Terra platform. The NRT product capitalizes on the unique attributes of the MISR aerosol retrieval approach and product contents, such as reliable aerosol optical depth as well as aerosol microphysical information. Several modifications are described that allow for rapid product generation within a three-hour window following acquisition of the satellite observations. Implications for the product quality and consistency are discussed as compared to the current operational L2 MISR aerosol product. Several ways of implementing additional use-specific retrieval screenings are also highlighted.

© 2021. California Institute of Technology. Government sponsorship acknowledged

## 1. Introduction

Atmospheric aerosols have for long been recognized to influence the climate, environment, and human health (e.g., IPCC, 2013; Lelieveld et al., 2015; Shindell et al., 2013; Turnock et al., 2020). They also affect satellite remote sensing of important geophysical parameters such as ocean color (e.g., Frouin et al., 2019; Gordon, 1997) or greenhouse gas abundance (Butz et al., 2009; Frankenberg et al., 2012; Houweling et al., 2005). Aerosol particles and their properties have been extensively studied in-situ and remotely: from the ground, in the air, and from space. These observational data vary in spatial and temporal coverage, but usually only offer snapshots of local conditions. Since atmospheric aerosols have a life cycle ranging from hours to days, numerical modeling of their emission, transport, and deposition has filled the coverage gaps and extended our understanding of their global impacts. This has given rise to a number of global aerosol reanalyses (Buchard et al., 2017; Gelaro et al., 2017; Inness et al., 2013, 2019; Lynch et al., 2016; Randles et al., 2017; Rienecker et al., 2011) that provide a long-range, gridded, and internally consistent outlook on aerosol burdens around the world. Furthermore, global aerosol modeling has been increasingly used for operational forecasting (e.g., Xian et al., 2019) and as support to decision making, for example in air quality alerts and in non-civilian applications (Liu et al., 2007).

The growing demand for consistent gridded aerosol products has been driving development and steady improvement of numerical predictions. [For example, the International Cooperation for Aerosol Prediction initiative was founded in 2010](#) (Benedetti et al., 2011; Reid et al., 2011), [with one of its goals being the development of global multi-model aerosol forecasting ensemble for basic research and operational use](#) (Xian et al., 2019). Still, models suffer from often poorly resolved aerosol emissions and sinks and can be affected by errors in the underlying meteorology. As a result, systematic and sampling-related biases in aerosol fields are often found between model simulations and satellite observations (e.g., Buchard et al., 2015; Colarco et al., 2010; Lamarque et al., 2013; Zhang and Reid, 2009). An effective way to mitigate some of these problems is by assimilating aerosol observations into numerical models (e.g., Bocquet et al., 2015; Fu et al., 2017; Sekiyama et al., 2010; Di Tomaso et al., 2017; Werner et al., 2019; Zhang et al., 2008). Satellite observations of aerosol optical and microphysical properties are inseparable from these data assimilation activities as they offer the necessary data volume, near-global coverage, and frequent repeat cycle. However, an often-considerable latency for generating science-quality “standard” satellite products (8 to 40 hours) renders them unsuitable for operational forecasting. This has led to the development of aerosol

products within the time frame required by modeling centers, usually three hours from satellite overpass. A number of near real-time (NRT) products has emerged.

Deleted: range

One example of a platform that provides users with NRT satellite products and imagery is NASA's Land, Atmosphere Near real-time Capability for EOS (LANCE) project (<https://earthdata.nasa.gov/earth-observation-data/near-real-time>). A range of instruments deliver various Level 1 (L1) and Level 2 (L2) data products (<https://earthdata.nasa.gov/collaborate/open-data-services-and-software/data-information-policy/data-levels>), including radiances, land surface properties, and atmospheric thermodynamics and composition within three hours from satellite observation. NRT aerosol products are currently available from the Moderate Resolution Imaging Spectroradiometer (MODIS), Ozone Monitoring Instrument (OMI), and Visible Infrared Imaging Radiometer Suite (VIIRS). NASA's Multi-angle Imaging SpectroRadiometer (MISR) currently provides NRT radiance and cloud motion vector products. The purpose of this paper is to introduce a new MISR NRT L2 aerosol product available within LANCE.

This paper is organized as follows. Section 2 and 3 provide brief descriptions of the MISR instrument and the data processing sequence, respectively. Section 4 first outlines the cloud identification methods employed in the MISR aerosol algorithm and then describes algorithmic modifications introduced in the NRT processing. Adjustments to cloud and retrieval screening parameters and their implications are discussed. The global distributions of the NRT product are analyzed in Section 5. Section 6 provides a summary.

## 2. MISR instrument and aerosol data product

The MISR instrument flies aboard the NASA Earth Observing System (EOS) Terra satellite, launched in December 1999 to a sun-synchronous descending polar orbit, at an orbital altitude of 705 km, an orbital period of 99 minutes, and an equatorial crossing time of 10:30 a.m. local time. MISR makes 14.56 orbits per day with a repetition cycle (revisit) of 16 days. The orbit tracks are georeferenced to a fixed set of 233 ground paths. With a cross-track swath of about 380 km, total Earth coverage is obtained every 9 days at the equator and every 2 days at high latitudes.

MISR contains nine pushbroom cameras with viewing angles at the Earth's surface ranging from 0° (nadir) to +/- 70.5° oriented along the direction of the flight track. A point on the ground is imaged by all nine cameras in approximately 7 minutes. The cameras make observations of reflected solar radiance in four spectral bands, centered at 446 (blue), 558

(green), 672 (red), and 866 (near-infrared) nm. The spatial resolution depends on the camera and wavelength. The red band has a full 275 m resolution in all cameras. The other three spectral channels are averaged onboard to a 1.1 km resolution in global-mode operation (Diner et al., 1998), with the exception of the nadir camera which preserves the full 275 m resolution in all spectral channels. See <https://misr.jpl.nasa.gov/Mission/> for more details.

MISR employs two processing pathways for aerosol retrievals, one for observations over land (Martonchik et al., 2009), and another for dark water (DW) (Kalashnikova et al., 2013), which applies over deep oceans, seas, and lakes. Previous versions of the MISR aerosol product were extensively validated over the years (e.g., Kahn et al., 2010; Kahn and Gaitley, 2015; Kalashnikova et al., 2013; Shi et al., 2014; Witek et al., 2013) showing high retrieval quality over land and ocean.

The current operational version of the MISR aerosol product, designated as version 23 (V23), was released publicly in June 2018. It introduced multiple algorithmic, data product, and data usability improvements (Garay et al., 2020; Witek et al., 2018a, 2018b). V23 provides aerosol information with a spatial resolution of 4.4 km x 4.4 km packaged in NetCDF-4 format. Initial validation efforts showed that V23 retrievals are more accurate than previous versions, with most pronounced improvements in the DW algorithm (Garay et al., 2020). V23 retrievals over oceans were extensively validated by Witek et al. (2019), indicating excellent agreement with ground-based observations. Other V23 Aerosol Optical Depth (AOD) evaluation efforts show similar results (e.g., Choi et al., 2019; Sayer et al., 2020; Si et al., 2020; Sogacheva et al., 2020). A first regional insight into retrieved particle properties from the MISR V23 aerosol product shows that MISR generally captures the distinct spatial and temporal features of aerosol type in East Asia (Tao et al., 2020). Furthermore, V23 has greatly improved the quality of reported AOD uncertainties, which now realistically represent retrieval errors (Sayer et al., 2020; Witek et al., 2019). This is especially relevant as pixel-level retrieval uncertainties are very important for satellite data assimilation, which is being increasingly used in aerosol modeling studies (Lynch et al., 2016; Shi et al., 2011, 2013; Zhang and Reid, 2010). MISR data and related documentation can be obtained from: <https://asdc.larc.nasa.gov/project/MISR>.

### 3. NRT latency and data description

MISR currently provides several L1 and L2 near real-time (NRT) radiance and cloud motion vector products (<https://earthdata.nasa.gov/earth-observation-data/near-real-time/download-nrt-data/misr-nrt>). All MISR NRT processing is based on Level 0 data downlinked in observational

132 sessions. These session-based files, representing portions of a single MISR orbit, usually cover  
133 between 10 to 50 minutes of observations, as compared to the full orbit period of 98.9 minutes.  
134 This session-based processing is necessary to allow for the fast product delivery required for  
135 NRT applications.

136 The new NRT L2 aerosol product file content, described in Data Product Specification  
137 ([https://asdc.larc.nasa.gov/documents/misr/DPS\\_AEROSOL\\_NRT\\_V023.20210430.pdf](https://asdc.larc.nasa.gov/documents/misr/DPS_AEROSOL_NRT_V023.20210430.pdf)), is  
138 equivalent to the standard aerosol product (Garay et al., 2020). The NRT L2 aerosol product file  
139 name convention is:

140 MISR\_AM1\_AS\_AEROSOL\_T{yyyymmddHHMMSS}\_P{ppp}\_O{oooooo}\_F13\_0023.nc, where  
141 'yyyy', 'mm', and 'dd' are the year, month, and day, and 'HH', 'MM' and 'SS' are the hour,  
142 minute, and seconds, respectively. Furthermore, {ppp} is the three-digit path identifier (between  
143 001 and 233) and {oooooo} is the six-digit orbit number. The NRT L2 aerosol product files are  
144 available for download within three hours of acquisition at NASA's Atmospheric Science Data  
145 Center (ASDC) (<https://asdc.larc.nasa.gov/project/MISR>).

146 For clarity, it is important to distinguish between the three different MISR L2 aerosol  
147 products: NRT, FIRSTLOOK, and standard aerosol (SA) product (see Figure 1). NRT is  
148 generated within a three-hour time interval after acquisition and uses the same ancillary inputs  
149 as FIRSTLOOK. These include the monthly gridded (1.0 degree) snow/ice mask and surface  
150 wind speed from the Terrestrial Atmospheric and Surface Climatology (TASC) database and the  
151 seasonal Radiometric Camera-by-camera Threshold Dataset (RCTD) (Diner et al., 1999a). Both  
152 NRT and FIRSTLOOK utilize TASC and RCTD datasets from the current month/season in the  
153 prior year. The FIRSTLOOK product is generated within two days from acquisition and includes  
154 cloud classification parameters obtained from the L1 and L2 cloud products. The SA product is  
155 available after final processing is performed on a seasonal basis and within three months past  
156 the end of the season, which results in a 3–6-month latency. The final processing utilizes the  
157 most recent snow/ice and wind speed data.

Deleted: ref

Formatted: Font color: Auto

Deleted: s

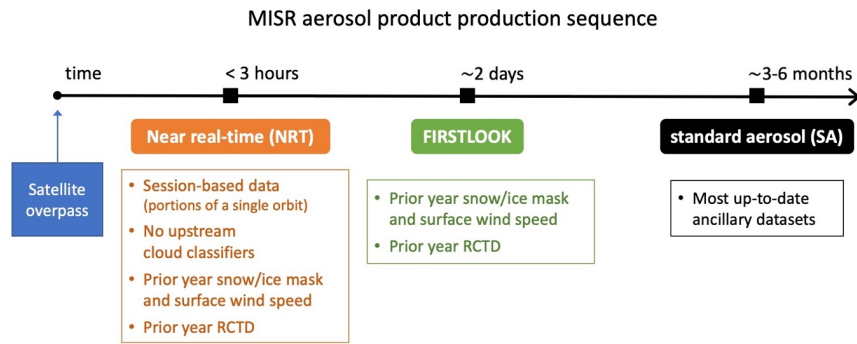


Figure 1 Schematic showing MISR aerosol product delivery timeline. Snow/ice mask and surface wind speed data are monthly averages. RCTD stands for Radiometric Camera-by-camera Threshold Dataset. MISR final production (SA) is processed on a seasonal cycle and is often delayed one to three months past the end of each season, which results in up to 6-month latency.

#### 4. Cloud screening in the NRT MISR aerosol product

Deleted: cloud screening

##### 4.1. Cloud identification

Identification of cloudy pixels is a critical element of all satellite aerosol remote sensing algorithms. MISR employs several cloud identification strategies which can be loosely split into two groups: the first group relies on cloud classifiers previously generated with MISR Level 2 Cloud Detection and Classification algorithm (Diner et al., 1999b), and the second group includes build-in tests that are internal to the aerosol retrieval algorithm (Diner et al., 2008).

##### 4.1.1. Upstream cloud classifiers

The operational MISR aerosol algorithm relies on a range of external input datasets that are either static—for example, a monthly wind speed climatology—or that need to be generated prior to aerosol retrievals in upstream processing. A notable example of such external inputs to the SA and FIRSTLOOK algorithms are cloud classification parameters obtained from the MISR L2 cloud product. An important implication of this dependency is that aerosol processing needs to wait for the cloud product to be generated, creating a time lag that is prohibitive for NRT applications. Typically, the L2 cloud product is generated within about 18 hours of overpass,

185 and the MISR L2 FIRSTLOOK aerosol processing is completed within about 2 days. In order to  
186 produce an L2 aerosol product within an about three-hour time frame, the algorithm needs to  
187 operate without the upstream cloud classifiers.

188 Two specific L2 cloud classification parameters utilized in [FIRSTLOOK and SA](#) aerosol  
189 processing are the MISR Stereoscopically-Derived Cloud Mask (SDCM) and the Angular  
190 Signature Cloud Mask (ASCM) (Diner et al., 1999b; Girolamo and Davies, 1994). In addition to  
191 these L2 products, the Radiometric Camera-by-camera Cloud Mask (RCCM) (Diner et al.,  
192 1999a; Girolamo and Davies, 1995) retrieved in L1B processing is also employed. All three  
193 parameters are reported at 1.1 km x 1.1 km resolution. It should be noted that RCCM also  
194 serves as an input to the algorithm that generates SDCM and ASCM, indicating that these  
195 parameters are not independent.

196 In the FIRSTLOOK and SA algorithm, the RCCM, SDCM, and ASCM cloud masks are  
197 used together to determine whether a particular 1.1 km x 1.1 km subregion is clear or cloudy.  
198 The implication is that if any of the 9 MISR cameras is designated as cloudy in a subregion, this  
199 subregion is excluded from aerosol retrieval. The clear/cloudy decision logic depends on the  
200 underlying surface type, assigned into three categories: land, water, and snow/ice. Generally, a  
201 “clear” outcome is favored over the two most frequently used surface types, land and water,  
202 assigning a subregion as cloudy only if the RCCM and SDCM masks indicate a cloud. The logic  
203 is considerably more conservative over snow/ice surfaces due to difficulties in distinguishing  
204 clouds from the underlying bright features. Details of the cloud mask decision logic over different  
205 surface types can be found in Diner et al. (2008).

206 Analyzing three months of V23 L2 [SA](#) product (March, April, May, 2020) indicates that  
207 the cloud masks along with the brightness test (see 4.1.2) lead to screening of about 50% of  
208 retrievals. As such, they have the largest impact on identifying and removing pixels where  
209 clouds might be present. These masks and decision pathways, however, have their deficiencies  
210 and additional checks were put in place to further decrease the frequency of cloud-  
211 contaminated aerosol retrievals.

212

#### 213 **4.1.2. Build-in cloud detection methods**

214

215 In addition to the cloud masks retrieved in the L1B processing (RCCM) and from the L2 Cloud  
216 Detection and Classification algorithm (SDCM, ASCM), the MISR aerosol retrieval algorithm  
217 relies on three internal tests to further identify cloudy pixels that might have escaped earlier  
218 detection. These are (1) the *brightness test*, (2) the *angle-to-angle smoothness test*, and (3) the

Deleted: aerosol

220 *angle-to-angle correlation test*. Details of these tests can be found in Diner et al. (2008) or Witek  
221 et al. (2013), but a short summary is provided here for completeness.

222 The brightness test is employed to identify clouds that lacked sufficient texture to be  
223 picked up by SDCM. For each surface type a fixed threshold is adopted on measured  
224 bidirectional reflectance factors (BRFs), and when exceeded in all spectral bands for at least  
225 one camera, it renders a subregion unsuitable for aerosol retrieval. The thresholds are set to  
226 1.0, 0.5, and 0.5 for snow/ice, land, and water surfaces, respectively. The value of 1.0 means  
227 that the brightness test is effectively turned off over snow/ice. Furthermore, the brightness test  
228 does not override subregions that were identified as clear by RCCM.

229 The angular smoothness test checks for unusually large variations in the measured  
230 equivalent reflectances as a function of camera angle, the premise being that in the absence of  
231 artifacts or subpixel clouds, the measured radiance should change smoothly from camera to  
232 camera. The test is achieved by fitting a polynomial to equivalent reflectances, separately for aft  
233 (+nadir) and forward (+nadir) cameras and each spectral band, and checking if the goodness of  
234 fit metric (definition in Diner et al., 2008) exceeds a threshold. If in at least one case the test  
235 fails, the subregion is eliminated.

236 Finally, the angle-to-angle correlation test also investigates radiance smoothness and  
237 correlation between camera angles, which makes it conceptually similar to the angular  
238 smoothness test, but instead utilizes high-resolution information from the red spectral band. It  
239 uses 4 x 4 arrays of the 275m spatial resolution red band equivalent reflectances in each 1.1 km  
240 x 1.1 km subregion. The test then evaluates spatial variability within the 4 x 4 array for each  
241 camera and compares it to a variability within a camera-average template. Variances,  
242 covariances, and normalized cross-correlations are calculated (see Diner et al., (2008) for  
243 details). If the variability within a camera deviates considerably from the average, this camera  
244 might have sub-pixel clouds or other contaminants, and as a result the subregion is excluded  
245 from aerosol retrievals.

246 In the three months of data analyzed in this study (March, April, May 2020), the relative  
247 occurrence of retrieval screening due the above-mentioned internal tests are about 4.0% and  
248 0.1% for the correlation and smoothness tests, respectively. These statistics come from  
249 analyzing the output field *Aerosol\_Retrieval\_Screening\_Flags* and as such they do not  
250 represent the absolute rates of success of each individual test. That is because the tests are  
251 performed in a sequential order and if one of them fails, tests that are next in sequence are not  
252 performed. For SA product generation, the order is: upstream cloud mask described in 4.1.1,  
253 the brightness test, the correlation test, and the smoothness test. For example, the correlation



test is only performed on pixels that already passed the upstream cloud tests as well as the brightness test. Additionally, the brightness test does not have its own flag in the *Aerosol\_Retrieval\_Screening\_Flags* output but is grouped together with the upstream cloud classifiers.

#### **4.2. Retrieval screening using regional cloud parameters**

Methods described in section 4.1 focus on identifying and excluding cloudy 1.1 km x 1.1 km subregions from the aerosol retrieval process. The retrieval region consists of 16 (4 x 4) subregions. These methods are highly effective at removing cloud-contaminated pixels, but since they rely on MISR visible wavelengths they might miss certain cloud signatures more easily detected in the infrared spectrum (e.g., Gao et al., 1993). For example, MODIS routinely uses its reflective and emissive infrared channels to detect optically thin cirrus clouds (Ackerman et al., 2010; Levy et al., 2013). As a result, MISR cloud detection methods occasionally fail, which leads to visible outliers in retrieved AODs (Witek et al., 2018b). For that reason, an additional set of screenings is applied in an effort to eliminate such unusually high AOD retrievals (Garay et al., 2020). Two of these additional methods look at overall cloudiness in the retrieval region (consisting of 4 x 4 subregions) as well as in a larger area consisting of 3 x 3 regions (12 x 12 subregions). The Cloud Screening Parameter (CSP) represents the fraction of clear grid cells within a region, whereas Cloud Screening Parameter Neighbor 3x3 (CSP9) is similar to CSP but for the larger area. If CSP is below 0.7 and CSP9 below 0.5, the retrieval is not reported in the final product intended for most users. However, it is still included in the product's AUXILIARY subcategory and annotated with the term "Raw" to indicate that the product has not undergone recommended quality screenings.

#### **4.3. Adjusting cloud screening thresholds**

##### **4.3.1. Performance of the prototype NRT product**

This subsection presents results and analysis of prototype NRT aerosol retrievals. These are obtained prior to any threshold and screening adjustments included in the final version of the product. To differentiate between the final and the prototype NRT products, the latter is denoted as  $NRT_{prot}$ .

As mentioned in the previous section, the NRT processing cannot rely on the cloud masks generated in the L1 and L2 cloud products, namely the RCCM, SDCM, and ASCM. This implies that potentially less screening of cloudy subregions would be applied, increasing the probability of cloud contamination in aerosol retrievals. However, some of the burden of cloud identification is picked up by the built-in cloud tests described in section 4.1.2. The frequency of these tests identifying cloudy pixels increases in NRT processing in comparison to standard processing, in large part mitigating the negative consequences resulting from the lack of the upstream cloud masks. This is well evidenced by examining the normalized probability density functions (*pdfs*) of AOD from spring 2020 (Figure 2). The SA (red) and NRT<sub>prot</sub> (blue) lines are very similar, indicating that the built-in cloud tests substitute to a significant extent for the missing upstream cloud masks in generating the NRT<sub>prot</sub> product. The largest difference occurs in the high-AOD range, suggesting that NRT<sub>prot</sub> has more retrievals in this regime. The black dotted line shows a *pdf* of the NRT<sub>prot</sub> AOD retrievals that do not have a matching SA retrieval. This is labeled as “NRT<sub>prot</sub> gained” as it represents additional retrievals obtained in NRT processing due to the lack of external cloud masks. The “NRT<sub>prot</sub> gained” *pdf* is clearly shifted towards higher AODs, confirming that the NRT<sub>prot</sub> processing tends to retrieve higher AODs in places where SA is not available.

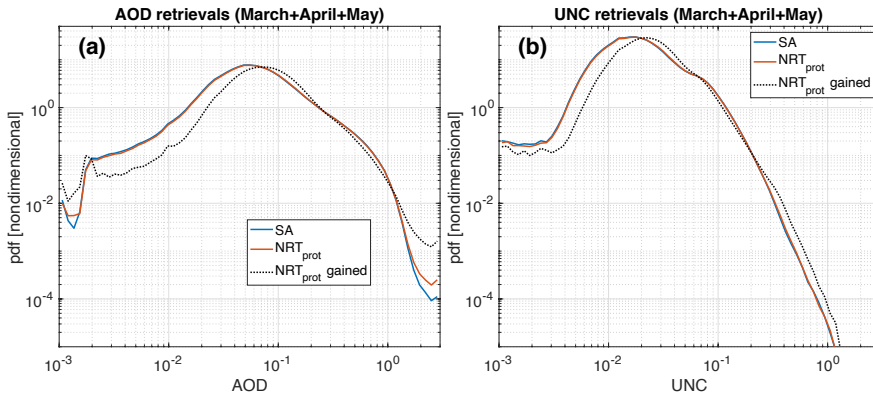
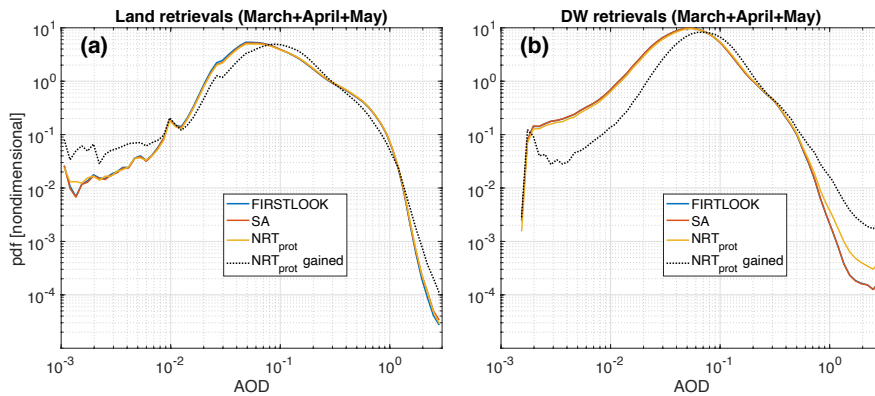


Figure 2 (a) AOD normalized probability density functions from SA, prototype NRT, and prototype NRT retrievals that do not have a matching SA equivalent (labeled as NRT<sub>prot</sub> gained); (b) same as in (a) but for retrieved AOD uncertainties (UNC). Data statistics for AODs are provided in Table 1.

Figure 3 shows *pdfs* of AOD but with retrievals separated between DW (Fig. 3a) and land (Fig. 3b). These *pdfs* indicate that the retrievals over oceans are the main source of

310 increased frequency of high-AODs in the NRT<sub>prot</sub> product. The *pdfs* over land are virtually  
 311 unchanged, including a slightly flattened but still relatively comparable distribution of the “NRT<sub>prot</sub>  
 312 gained” retrievals (Fig. 3b). The additional statistics of the data presented in Figs. 2 and 3,  
 313 including the retrieval count, the mean AOD, and the geometric mean AOD, which is better  
 314 suited for log-normal distributions of AOD (Sayer and Knobelspiesse, 2019), are provided in  
 315 Table 1. Note that the number of NRT<sub>prot</sub> gained is not the same as the number of NRT<sub>prot</sub> minus  
 316 SA. This is because some SA retrievals do not have their NRT<sub>prot</sub> equivalent, making the SA  
 317 count larger than it would have been otherwise.

318 In the 3-month period analyzed in this study (March, April, May, 2020), the NRT<sub>prot</sub>  
 319 processing leads to about 6.4% more retrievals than SA (see Table 1). 5.5 million NRT<sub>prot</sub>  
 320 retrievals do not have a matching SA retrieval (NRT gained), and the majority of them (67%) are  
 321 DW retrievals. The overall geometric means are almost identical in SA and NRT<sub>prot</sub>, although  
 322 small variations in this statistic are seen in DW and land categories. The NRT gained have  
 323 visibly higher mean and geometric mean values, the increase coming mainly from DW  
 324 retrievals. These basic statistics warrant a further look at the NRT<sub>prot</sub> performance over DW.



325  
 326 Figure 3 AOD pdfs for land (a) and DW (b) retrievals, respectively. Data statistics are provided in Table 1.

|                   | All retrievals |                     |                            | DW   |                     |                            | Land |                     |                            |
|-------------------|----------------|---------------------|----------------------------|------|---------------------|----------------------------|------|---------------------|----------------------------|
|                   | SA             | NRT <sub>prot</sub> | NRT <sub>prot</sub> gained | SA   | NRT <sub>prot</sub> | NRT <sub>prot</sub> gained | SA   | NRT <sub>prot</sub> | NRT <sub>prot</sub> gained |
| $N (\times 10^6)$ | 49.7           | 52.9                | 5.5                        | 27.6 | 30.7                | 3.7                        | 22.1 | 22.2                | 1.8                        |

|                |       |       |       |       |       |       |       |       |       |
|----------------|-------|-------|-------|-------|-------|-------|-------|-------|-------|
| <i>mean</i>    | 0.168 | 0.169 | 0.171 | 0.111 | 0.115 | 0.146 | 0.240 | 0.243 | 0.224 |
| <i>geomean</i> | 0.111 | 0.112 | 0.122 | 0.083 | 0.085 | 0.106 | 0.160 | 0.162 | 0.161 |

Table 1 Additional statistics for the data presented in Figs. 2 and 3 (statistic for FIRSTLOOK not shown). NRT gained stands for the prototype NRT retrievals that do not have a matching SA equivalent; geomean stands for the geometric mean AOD.

#### 4.3.2. Sensitivity to CSP and CSP9 thresholds in DW retrievals

One way to screen potentially cloud-contaminated high-AOD retrievals is to adjust thresholds on CSP and CSP9 parameters (Garay et al., 2020). This is furthermore justified by the fact that in the absence of RCCM, SDCM, and ASCM in NRT<sub>prot</sub> processing, fewer cloudy subregions are identified in a retrieval area and consequently CSP and CSP9 have by default lower values. This argument provides strong justification for investigating sensitivity to increased CSP and CSP9 thresholds in the NRT<sub>prot</sub> processing.

The SA product uses the thresholds of CSP=0.7 and CSP9=0.5 (Garay et al., 2020); when the values of CSP and CSP9 are below these thresholds in a retrieval region, the aerosol retrieval is removed from the data field recommended for users. Figure 4 and Table 2 show *pdfs* and AOD statistics for different thresholds of CSP and CSP9 parameters in the NRT<sub>prot</sub> product over dark water surfaces. There are only minor changes in the *pdfs* when the thresholds are increased, including in the high-AOD regime. The mean and geometric mean decrease gradually but slowly; even at the highest considered thresholds (0.85 for CSP and 0.75 for CSP9) these statistics are still above the SA values. At the same time the number of passing NRT<sub>prot</sub> retrievals decreases considerably faster, with almost 19% of retrievals lost when the highest thresholds are used. These results indicate that adjusting CSP and CSP9 thresholds is not an effective strategy to constraining NRT<sub>prot</sub> retrievals.

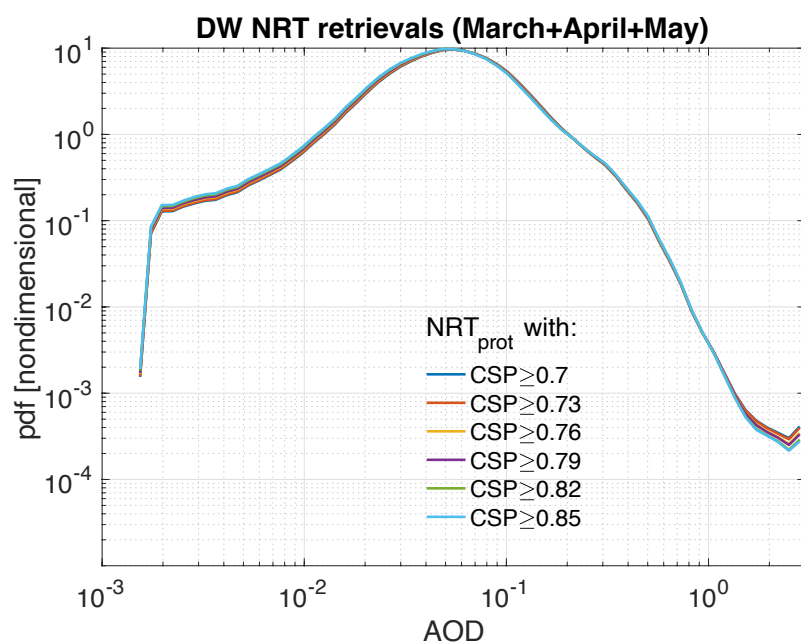


Figure 4 Prototype NRT AOD pdfs over dark water surfaces from spring 2020 obtained with different CSP and CSP9 cloud-screening thresholds. Data statistics are provided in Table 2.

|                   |                        |                        |                        |                        |                        |                        |                        |
|-------------------|------------------------|------------------------|------------------------|------------------------|------------------------|------------------------|------------------------|
| $N (\times 10^6)$ | 30.7                   | 30.1<br>(-1.9%)        | 28.4<br>(-7.4%)        | 27.7<br>(-9.8%)        | 25.9<br>(-15.6%)       | 24.9<br>(-18.9%)       | SA<br>27.6             |
| CSP               | $\geq 0.7$             | $\geq 0.73$            | $\geq 0.76$            | $\geq 0.79$            | $\geq 0.82$            | $\geq 0.85$            |                        |
| CSP9              | $\geq 0.5$             | $\geq 0.55$            | $\geq 0.6$             | $\geq 0.65$            | $\geq 0.7$             | $\geq 0.75$            |                        |
| mean              | 0.1151<br>$\pm 0.1200$ | 0.1149<br>$\pm 0.1199$ | 0.1145<br>$\pm 0.1190$ | 0.1144<br>$\pm 0.1191$ | 0.1142<br>$\pm 0.1185$ | 0.1143<br>$\pm 0.1189$ | 0.1110<br>$\pm 0.1079$ |
| geomean           | 0.0850                 | 0.0847                 | 0.0841                 | 0.0839                 | 0.0834                 | 0.0832                 | 0.0826                 |

Table 2 Additional statistics for the data presented in Fig. 4. Values for CSP and CSP9 indicate their corresponding thresholds for screening AOD retrievals. The arithmetic mean values are accompanied by their respective  $\pm$  one standard deviations.

#### 4.3.3. Sensitivity to ARCI threshold in DW retrievals

357 V23 of the MISR aerosol product introduced a new parameter, called the aerosol retrieval  
358 confidence index (ARCI), that is used to screen high-AOD retrieval outliers caused by cloud  
359 contamination and other factors (Witek et al., 2018b). ARCI, defined only for DW retrievals,  
360 proved to be an efficient metric at filtering out potentially cloud-contaminated AOD retrievals. In  
361 standard processing, retrievals with  $ARCI < 0.15$  are removed from the recommended user  
362 field, but are retained in the AUXILIARY group. The 0.15 threshold is well supported through  
363 statistical analysis (Witek et al., 2018b), although some erroneous AODs still pass this  
364 screening method, suggesting that increasing this threshold might be beneficial in NRT  
365 processing.

366 Figure 5 and Table 3 show *pdfs* and AOD statistics for different thresholds of ARCI in the  
367 NRT<sub>prot</sub> product. In this case the differences between ARCI thresholds are quite noticeable,  
368 especially in the high-AOD range of retrievals. Increasing the ARCI threshold to 0.2 leads to a  
369 loss of about 11% of NRT<sub>prot</sub> DW retrievals, but the resulting mean and geometric mean are  
370 lower than the SA values. At the same time, the absolute number of NRT<sub>prot</sub> DW retrievals (27.4  
371 million) is still comparable to the number of SA DW retrievals (27.6 million). The *pdfs* and the  
372 statistics suggest that increasing the NRT<sub>prot</sub> ARCI threshold from 0.15 to 0.18 leads to a  
373 product that has similar characteristics to SA.

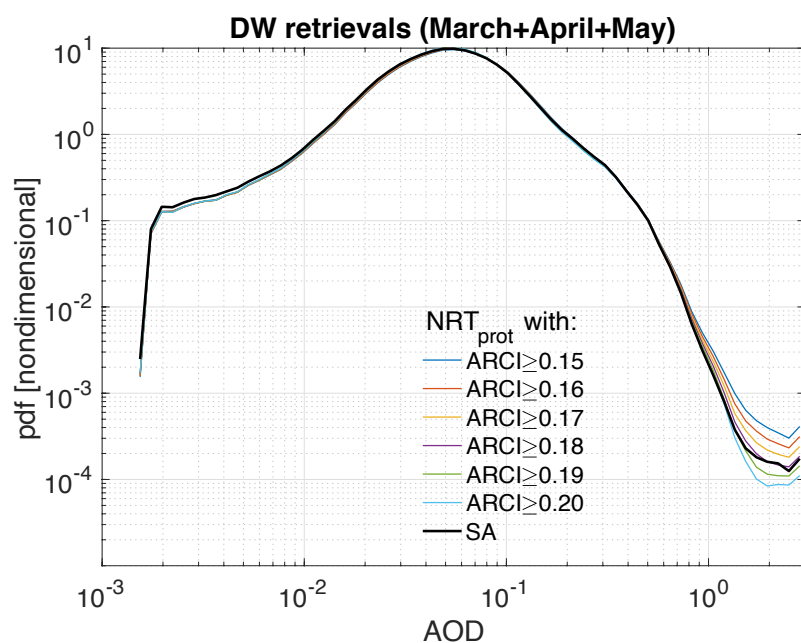


Figure 5 Prototype NRT AOD pdfs from spring 2020 obtained with different ARCI thresholds. Data statistic are provided in Table 3.

|                   |                        |                        |                        |                        |                        |                        |                        |
|-------------------|------------------------|------------------------|------------------------|------------------------|------------------------|------------------------|------------------------|
| $N (\times 10^6)$ | 30.7                   | 30.0<br>(-2.2%)        | 29.4<br>(-4.3%)        | 28.7<br>(-6.5%)        | 28.0<br>(-8.6%)        | 27.4<br>(-10.8%)       | SA<br>27.6             |
| ARCI              | $\geq 0.15$            | $\geq 0.16$            | $\geq 0.17$            | $\geq 0.18$            | $\geq 0.19$            | $\geq 0.20$            |                        |
| mean              | 0.1151<br>$\pm 0.1200$ | 0.1137<br>$\pm 0.1157$ | 0.1124<br>$\pm 0.1122$ | 0.1112<br>$\pm 0.1094$ | 0.1100<br>$\pm 0.1070$ | 0.1090<br>$\pm 0.1051$ | 0.1110<br>$\pm 0.1079$ |
| geomean           | 0.0850                 | 0.0842                 | 0.0835                 | 0.0828                 | 0.0821                 | 0.0813                 | 0.0826                 |

Table 3 Additional statistic for the data presented in Fig. 5.

#### 4.3.4. Recommendation for NRT processing

The statistical analyses presented in the previous sections indicate that the lack of RCCM, SDCM, and ASCM in NRT processing has negative consequences on the product, especially by

allowing more, potentially cloud-contaminated, high-AOD DW retrievals to pass screening criteria. Adjusting build-in cloud screening thresholds on CSP and CSP9 brings only limited benefits at the cost of losing a considerable percentage of retrievals. However, the ARCI threshold adjustments result in much closer statistical correspondence between the  $NRT_{prot}$  and standard AOD retrievals. For that reason, a revised ARCI threshold of 0.18 is implemented in NRT processing. Since the unscreened retrievals, as well as the ARCI parameter, are also provided in the AUXILIARY group of the product, users are encouraged to experiment with their own thresholds which might prove more beneficial in specific applications or geographic areas.

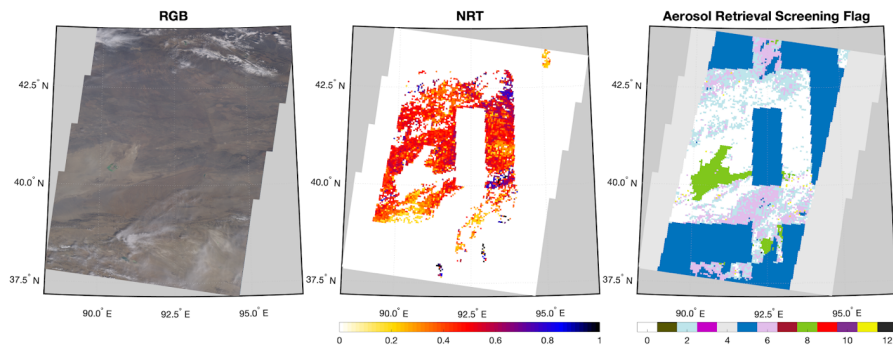
#### 4.4. Cloud/clear decision logic over snow/ice

In section 4.1.1 the impact of upstream cloud classifiers in standard processing—namely the RCCM, SDCM, and ASCM—on the subregion's cloud/clear designation was briefly described. The decision pathway depends on the underlying surface type, which can be either land, water, or snow/ice. Over land and water, the “cloud” outcome is only obtained when both RCCM and SDCM designate the subregion as cloudy. In the absence of RCCM and SDCM the default outcome is “clear”. Over snow/ice, however, the logic is more restrictive and favors the “cloudy” designation (Diner et al., 2008). Specifically, when the upstream cloud classifiers are not available, the subregion designation is set to “cloudy” by default. This has important implications on aerosol retrievals in areas where snow and ice occur seasonally.

The snow/ice surface mask, unlike land and water, is not static and changes every month. Furthermore, the snow/ice mask input to MISR aerosol processing has a 1.0-degree horizontal resolution, which is re-gridded to a 1.1 km resolution corresponding to the resolution of MISR subregion. In FIRSTLOOK processing, the snow/ice mask from the same month but in the previous year is used. The final SA processing is performed when the current year's monthly snow/ice mask becomes available. The NRT processing, similarly to FIRSTLOOK, relies on the previous year's snow/ice mask. Additionally, given the lack of upstream cloud classifiers, the snow/ice areas are designated as “cloudy” for aerosol retrieval purposes. This is well visualized in Figure 6 which shows the visible image and the corresponding maps of AOD and Aerosol Retrieval Screening Flag in the NRT processing. The dark blue color (index 5) denotes cloudy regions determined using the snow/ice cloud logic. The box-like nature of the excluded areas is associated with the coarse resolution of the snow/ice mask (1.0 degree). The previous year's mask might also not be representative of the current conditions on the ground. It is worth noting that the FIRSTLOOK product often suffers from the same exclusion rules as NRT. This is



417 because of the strict clear/cloud logic over snow/ice surfaces which favors the cloudy outcome;  
 418 in the case shown in Fig. 6 the AOD gaps in FIRSTLOOK (not shown) look very similar to the  
 419 NRT product.



420  
 421 *Figure 6 Example of snow/ice masking in NRT AOD retrievals. (Left) Visible image of the retrieval area. (Center) Corresponding*  
 422 *NRT AOD retrievals. (Right) NRT Aerosol Retrieval Screening Flag for the same area; the dark blue color denotes regions*  
 423 *designated as cloudy.*

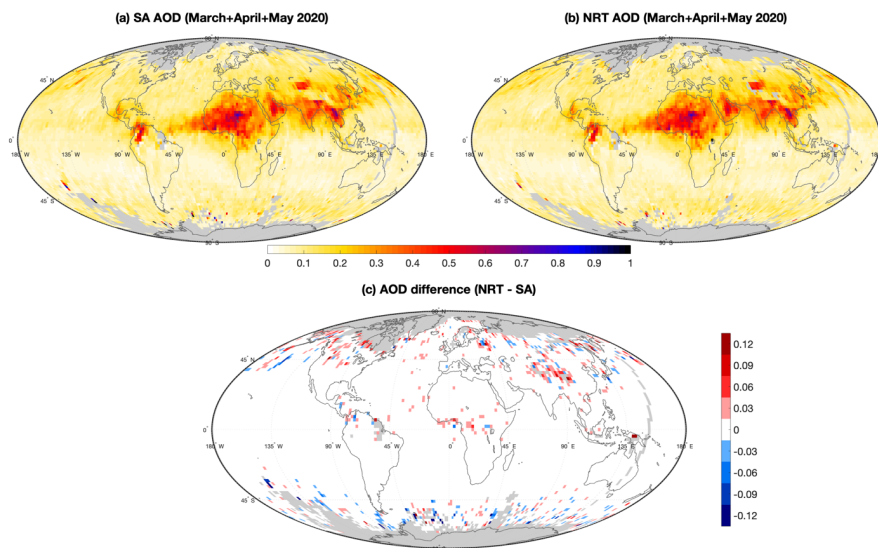
424 Several attempts have been made by the MISR science team to improve NRT aerosol  
 425 retrievals in snow/ice covered areas. However, identifying and isolating snow-covered surfaces  
 426 in the absence of upstream cloud classifiers proves very challenging. The quality of aerosol  
 427 retrievals is often negatively affected in such conditions. For that reason, and in an attempt to  
 428 eliminate as many NRT AOD outliers as possible, the current snow/ice logic is retained in the  
 429 NRT aerosol processing.

### 430 431 **5. NRT and SA differences**

432  
 433 In this section, geographic distributions of MISR AOD retrievals from SA and NRT products are  
 434 analyzed. The datasets encompass three months, March, April, and May of 2020. The NRT  
 435 AOD retrievals are screened with the revised ARCI threshold of 0.18 as suggested in section  
 436 4.3.4. The spatial overlap of the SA and NRT data is achieved using an intersect of the X\_Dim  
 437 and Y\_Dim fields in the two data products.

438 Figure 7 shows the global distributions of geometric mean AOD from the (a) SA and (b)  
 439 NRT products. The retrievals are gridded at 2-by-2-degree spatial resolution. Fig. 7c shows the  
 440 AOD difference between the two products (NRT – SA).

441 The largest AOD differences are seen in areas with climatologically high cloud cover,  
 442 especially over the Southern Ocean, and over land in areas where potential snow cover could  
 443 be an issue. Over the Southern Ocean the SA AODs are predominantly higher than the NRT  
 444 AODs. This is due to the increased ARCI threshold in NRT (0.18 vs. 0.15 in SA) which brings in  
 445 more aggressive screening of cloud-contaminated retrievals (Witek et al., 2018b). Over land,  
 446 where the ARCI parameter is not available, the gridded NRT AODs tend to be higher than the  
 447 SA AODs, which is in part related to the differences in snow/ice mask between the two  
 448 products. Still, the AOD differences in Fig. 7c are rather small and reflect sampling issues rather  
 449 than any systematic deficiencies in NRT processing. At the same time the lack of cloud  
 450 classifiers in NRT does not adversely affect AOD distributions, which is consistent with the  
 451 statistical analysis presented in section 4.2.3.



452  
 453 *Figure 7 (a) Global distribution of SA AOD geometric mean values across March, April, and May of 2020 on a 2-by-2-degree*  
 454 *spatial resolution; (b) same as in (a) but for NRT AOD; and (c) AOD difference between SA and NRT. Grid points with less than 15*  
 455 *retrievals are excluded.*

456 Figure 8 complements Fig. 7 by showing (a) the SA retrieval count distribution as well as  
 457 (b) the retrieval count difference between the SA and NRT products.

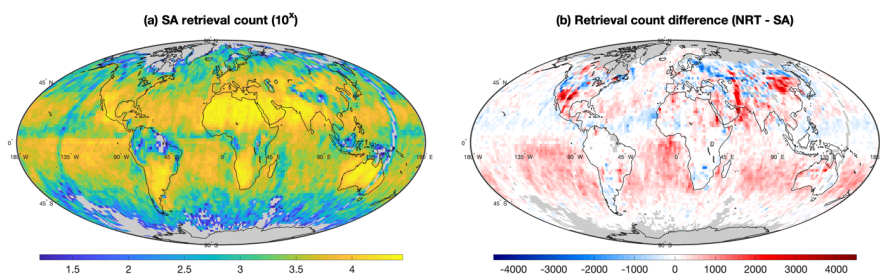


Figure 8 (a) Decimal logarithm of the retrieval count from the SA product in March, April, and May of 2020; (b) retrieval count difference between SA and NRT. Presented values are gridded at 2-by-2-degree spatial resolution and grid points with less than 15 retrievals are excluded.

The highest number of retrievals is found over the subtropical continents where the cloud cover is usually the smallest. Over the subtropical oceans in the Southern Hemisphere the NRT retrieval counts are typically higher than in SA, which results from the absence of upstream cloud classifiers in NRT processing and subsequently fewer subregions being excluded as cloudy. Note that this increase in retrieval count caused by the lack of cloud classifiers is not compensated by the increased ARCI threshold in NRT processing ( $\text{ARCI} \geq 0.18$ ), which always reduces the number of retrievals when compared to the default SA threshold ( $\text{ARCI} \geq 0.15$ ). The lack of hemispheric symmetry in this case is likely due to the seasonal variability (only months in northern spring are analyzed here). Over land the lack of upstream cloud classifiers also results in higher number of NRT retrievals in certain regions, but the surface type exclusion rules reverse this pattern, especially at higher latitudes. The conservative cloud logic over snow/ice surfaces in NRT processing often results in the lower number of NRT retrievals in the high latitudes of the northern hemisphere.

## 6. Summary

The MISR V23 aerosol product, publicly available since mid-2018, is a high-resolution state-of-the-art data product from NASA's Terra flagship mission. V23 AOD retrievals have remarkable accuracy compared against ground-based observations (Garay et al., 2020; Tao et al., 2020; Witek et al., 2019) and the product is more intuitive and easier to use than previous versions. The product is available within 2 days from satellite overpass as a FIRSTLOOK version, and within 3-to-6 months as a final science-quality SA version that employs the most up-to-date

484 ancillary datasets. In response to the needs of operational user communities, a new MISR L2  
485 NRT aerosol product has been developed with a 3-hour latency.

486 The new NRT algorithm does not depend on the upstream cloud classifiers that are  
487 generated in L1 and L2 cloud processing. The lack of cloud classifiers is in large part mitigated  
488 by the aerosol algorithm's built-in cloud identification methods. Analysis of the prototype NRT  
489 product has shown an increased frequency of high-AOD retrievals, especially over oceans and  
490 in climatologically cloudy areas, likely due to an increase in cloud contamination. Adjusting the  
491 ARCI threshold in DW retrievals proves highly effective at eliminating some of these high-AOD  
492 outliers and improves the NRT product's statistical agreement with the SA version. The new  
493 NRT aerosol product applies an ARCI threshold of 0.18 to mitigate cloud contamination in the  
494 absence of upstream cloud masks in NRT processing. The remaining differences in statistical  
495 and geographic distributions between the NRT and SA AODs, which includes information from  
496 the L2 cloud product, are small and largely confined to areas with high cloud cover.

497 The results of this study also serve as an example of the effects of screening threshold  
498 adjustments in MISR aerosol retrievals on AOD statistics and distributions. Researchers  
499 interested in particular applications and/or specific geographic regions are encouraged to  
500 experiment with their own threshold to achieve most optimal results. The NRT aerosol product  
501 contains both the recommended product contained within the main science directory  
502 "4.4\_KM\_PRODUCTS" that has the stricter ARCI threshold ( $\text{ARCI} \geq 0.18$ ), and the unscreened  
503 product without the additional cloud and ARCI filtering designed for more experienced users,  
504 located within the AUXILIARY group.

505

## 506 **Acknowledgements**

507 This research was carried out at the Jet Propulsion Laboratory, California Institute of  
508 Technology, under a contract with the National Aeronautics and Space Administration. Support  
509 from the MISR project is acknowledged. All data analyzed in this study are publicly available,  
510 although the transient nature of NRT products might limit their availability. The data can be  
511 downloaded from <https://l0dup05.larc.nasa.gov/cgi-bin/MISR/main.cgi>.

512

513

514 **References:**

- 515 Ackerman, S., Richard, F., Kathleen, S., Yinghui, L., Liam, G., Bryan, B. and Paul, M.:  
516 Discriminating clear-sky from cloud with MODIS algorithm theoretical basis document  
517 (MOD35), Univ. Wisconsin - Madison, 6th Edn.(October), 129 [online] Available from:  
518 <http://citeseerx.ist.psu.edu/viewdoc/summary?doi=10.1.1.385.4885>, 2010.
- 519 Benedetti, A., Reid, J. S. and Colarco, P. R.: International cooperative for aerosol prediction  
520 workshop on aerosol forecast verification, in Bulletin of the American Meteorological Society,  
521 vol. 92., 2011.
- 522 Bocquet, M., Elbern, H., Eskes, H., Hirtl, M., Aabkar, R., Carmichael, G. R., Flemming, J.,  
523 Inness, A., Pagowski, M., Pérez Camacho, J. L., Saide, P. E., San Jose, R., Sofiev, M., Vira, J.,  
524 Baklanov, A., Carnevale, C., Grell, G. and Seigneur, C.: Data assimilation in atmospheric  
525 chemistry models: Current status and future prospects for coupled chemistry meteorology  
526 models, *Atmos. Chem. Phys.*, 15(10), 5325–5358, doi:10.5194/acp-15-5325-2015, 2015.
- 527 Buchard, V., Da Silva, A. M., Colarco, P. R., Darmenov, A., Randles, C. A., Govindaraju, R.,  
528 Torres, O., Campbell, J. and Spurr, R.: Using the OMI aerosol index and absorption aerosol  
529 optical depth to evaluate the NASA MERRA Aerosol Reanalysis, *Atmos. Chem. Phys.*, 15(10),  
530 5743–5760, doi:10.5194/acp-15-5743-2015, 2015.
- 531 Buchard, V., Randles, C. A., da Silva, A. M., Darmenov, A., Colarco, P. R., Govindaraju, R.,  
532 Ferrare, R., Hair, J., Beyersdorf, A. J., Ziemba, L. D. and Yu, H.: The MERRA-2 aerosol  
533 reanalysis, 1980 onward. Part II: Evaluation and case studies, *J. Clim.*, 30(17),  
534 doi:10.1175/JCLI-D-16-0613.1, 2017.
- 535 Butz, A., Hasekamp, O. P., Frankenberg, C. and Aben, U.: Retrievals of atmospheric CO<sub>2</sub> from  
536 simulated space-borne measurements of backscattered near-infrared sunlight: Accounting for  
537 aerosol effects, *Appl. Opt.*, 48, 3322–3336, doi:10.1364/AO.48.003322, 2009.
- 538 Choi, M., Lim, H., Kim, J., Lee, S., Eck, T. F., Holben, B. N., Garay, M. J., Hyer, E. J., Saide, P.  
539 E. and Liu, H.: Validation, comparison, and integration of GOCI, AHI, MODIS, MISR, and  
540 VIIRS aerosol optical depth over East Asia during the 2016 KORUS-AQ campaign, *Atmos.*

541 Meas. Tech., 12(8), 4619–4641, doi:10.5194/amt-12-4619-2019, 2019.

542 Colarco, P., Da Silva, A., Chin, M. and Diehl, T.: Online simulations of global aerosol  
543 distributions in the NASA GEOS-4 model and comparisons to satellite and ground-based aerosol  
544 optical depth, *J. Geophys. Res. Atmos.*, 115(14), doi:10.1029/2009JD012820, 2010.

545 Diner, D. J., Beckert, J. C., Reilly, T. H., Bruegge, C. J., Conel, J. E., Kahn, R. A., Martonchik,  
546 J. V., Ackerman, T. P., Davies, R., Gerstl, S. A. W., Gordon, H. R., Muller, J. P., Myneni, R. B.,  
547 Sellers, P. J., Pinty, B. and Verstraete, M. M.: Multiangle Image Spectroradiometer (MISR)  
548 instrument description and experiment overview, *IEEE Trans. Geosci. Remote Sens.*, 36(4),  
549 1072–1087, 1998.

550 Diner, D. J., Di Girolamo, L. and Clothiaux, E. E.: Level 1 Cloud Detection Algorithm  
551 Theoretical Basis, *Jet Propuls. Lab. Calif. Inst. Technol.*, D-13397(Rev. B), 1999a.

552 Diner, D. J., Davies, R., Di Girolamo, L., Horvath, A., Moroney, C., Muller, J. P., Paradise, S.  
553 R., Wenkert, D. and Zong, J.: Level 2 Cloud Detection and Classification Algorithm Theoretical  
554 Basis, *Jet Propuls. Lab. Calif. Inst. Technol.*, D-11399(Rev. D), 1999b.

555 Diner, D. J., Abdou, W. A., Ackerman, T. P., Crean, K., Gordon, H. R., Kahn, R. A.,  
556 Martonchik, J. V., McMurdock, S., Paradise, S. R. and Pinty, B.: Level 2 aerosol retrieval  
557 algorithm theoretical basis, *Jet Propuls. Lab. Calif. Inst. Technol.*, D-11400(Rev. G), 2008.

558 Frankenberg, C., Hasekamp, O., O'Dell, C., Sanghavi, S., Butz, A. and Worden, J.: Aerosol  
559 information content analysis of multi-angle high spectral resolution measurements and its benefit  
560 for high accuracy greenhouse gas retrievals, *Atmos. Meas. Tech.*, 5(7), 1809–1821,  
561 doi:10.5194/amt-5-1809-2012, 2012.

562 Frouin, R. J., Franz, B. A., Ibrahim, A., Knobelspiesse, K., Ahmad, Z., Cairns, B., Chowdhary,  
563 J., Dierssen, H. M., Tan, J., Dubovik, O., Huang, X., Davis, A. B., Kalashnikova, O., Thompson,  
564 D. R., Remer, L. A., Boss, E., Coddington, O., Deschamps, P. Y., Gao, B. C., Gross, L.,  
565 Hasekamp, O., Omar, A., Pelletier, B., Ramon, D., Steinmetz, F. and Zhai, P. W.: Atmospheric  
566 Correction of Satellite Ocean-Color Imagery During the PACE Era, *Front. Earth Sci.*, 7,  
567 doi:10.3389/feart.2019.00145, 2019.

568 Fu, G., Prata, F., Xiang Lin, H., Heemink, A., Segers, A. and Lu, S.: Data assimilation for  
 569 volcanic ash plumes using a satellite observational operator: A case study on the 2010  
 570 Eyjafjallajökull volcanic eruption, *Atmos. Chem. Phys.*, 17(2), 1187–1205, doi:10.5194/acp-17-  
 571 1187-2017, 2017.

572 Gao, B. C., Goetz, A. F. H. and Wiscombe, W. J.: Cirrus cloud detection from Airborne Imaging  
 573 Spectrometer data using the 1.38  $\mu\text{m}$  water vapor band, *Geophys. Res. Lett.*, 20(3), 301–304,  
 574 doi:10.1029/93GL00106, 1993.

575 Garay, M. J., Witek, M. L., Kahn, R. A., Seidel, F. C., Limbacher, J. A., Bull, M. A., Diner, D.  
 576 J., Hansen, E. G. E. G., Kalashnikova, O. V., Lee, H., Nastan, A. M. and Yu, Y.: Introducing the  
 577 4.4km spatial resolution Multi-Angle Imaging SpectroRadiometer (MISR) aerosol product,  
 578 *Atmos. Meas. Tech.*, 13(2), 593–628, doi:10.5194/amt-13-593-2020, 2020.

579 Gelaro, R., McCarty, W., Suárez, M. J., Todling, R., Molod, A., Takacs, L., Randles, C. A.,  
 580 Darmenov, A., Bosilovich, M. G., Reichle, R., Wargan, K., Coy, L., Cullather, R., Draper, C.,  
 581 Akella, S., Buchard, V., Conaty, A., da Silva, A. M., Gu, W., Kim, G. K., Koster, R., Lucchesi,  
 582 R., Merkova, D., Nielsen, J. E., Partyka, G., Pawson, S., Putman, W., Rienecker, M., Schubert,  
 583 S. D., Sienkiewicz, M. and Zhao, B.: The modern-era retrospective analysis for research and  
 584 applications, version 2 (MERRA-2), *J. Clim.*, 30(14), 5419–5454, doi:10.1175/JCLI-D-16-  
 585 0758.1, 2017.

586 Girolamo, L. Di and Davies, R.: A Band-Differenced Angular Signature Technique for Cirrus  
 587 Cloud Detection, *IEEE Trans. Geosci. Remote Sens.*, 32(4), 890–896, doi:10.1109/36.298017,  
 588 1994.

589 Girolamo, L. Di and Davies, R.: The Image Navigation Cloud Mask for the Multiangle Imaging  
 590 Spectroradiometer (MISR), *J. Atmos. Ocean. Technol.*, 12(6), doi:10.1175/1520-  
 591 0426(1995)012<1215:tincmf>2.0.co;2, 1995.

592 Gordon, R.: Atmospheric correction of ocean color imagery in the Earth Observing System era,  
 593 *J. Geophys. Res. - Atmos.*, 102(D14), 17081–17106, doi:10.1029/96JD02443, 1997.

594 Houweling, S., Hartmann, W., Aben, I., Schrijver, H., Skidmore, J., Roelofs, G. J. and Breon, F.

595 M.: Evidence of systematic errors in SCIAMACHY-observed CO<sub>2</sub> due to aerosols, *Atmos.*  
596 *Chem. Phys.*, 5(11), 3003–3013, doi:10.5194/acp-5-3003-2005, 2005.

597 Inness, A., Baier, F., Benedetti, A., Bouarar, I., Chabrillat, S., Clark, H., Clerbaux, C., Coheur,  
598 P., Engelen, R. J., Errera, Q., Flemming, J., George, M., Granier, C., Hadji-Lazaro, J., Huijnen,  
599 V., Hurtmans, D., Jones, L., Kaiser, J. W., Kapsomenakis, J., Lefever, K., Leitão, J., Razinger,  
600 M., Richter, A., Schultz, M. G., Simmons, A. J., Suttie, M., Stein, O., Thépaut, J. N., Thouret,  
601 V., Vrekoussis, M. and Zerefos, C.: The MACC reanalysis: An 8 yr data set of atmospheric  
602 composition, *Atmos. Chem. Phys.*, 13(8), 4073–4109, doi:10.5194/acp-13-4073-2013, 2013.

603 Inness, A., Ades, M., Agustí-Panareda, A., Barré, J., Benedictow, A., Blechschmidt, A.-M.,  
604 Dominguez, J. J., Engelen, R., Eskes, H., Flemming, J., Huijnen, V., Jones, L., Kipling, Z.,  
605 Massart, S., Parrington, M., Peuch, V.-H., Razinger, M., Remy, S., Schulz, M. and Suttie, M.:  
606 The CAMS reanalysis of atmospheric composition, *Atmos. Chem. Phys.*, 19(6), 3515–3556,  
607 doi:10.5194/acp-19-3515-2019, 2019.

608 IPCC: Climate Change 2013: The Physical Science Basis. Contribution of Working Group I to  
609 the Fifth Assessment Report of the Intergovernmental Panel on Climate Change, edited by T. F.  
610 Stocker, D. Qin, G. K. Plattner, M. M. B. Tignor, S. K. Allen, J. Boschung, A. Nauels, Y. Xia,  
611 V. Bex, and P. M. Midgley, Cambridge University Press, Cambridge, United Kingdom and New  
612 York, NY, USA., 2013.

613 Kahn, R. A. and Gaitley, B. J.: An analysis of global aerosol type as retrieved by MISR, J.  
614 *Geophys. Res. Atmos.*, 120(9), 4248–4281, doi:10.1002/2015JD023322, 2015.

615 Kahn, R. A., Gaitley, B. J., Garay, M. J., Diner, D. J., Eck, T. F., Smirnov, A. and Holben, B. N.:  
616 Multiangle Imaging SpectroRadiometer global aerosol product assessment by comparison with  
617 the Aerosol Robotic Network, *J. Geophys. Res. Atmos.*, 115(23), doi:10.1029/2010JD014601,  
618 2010.

619 Kalashnikova, O. V., Garay, M. J., Martonchik, J. V. and Diner, D. J.: MISR Dark Water aerosol  
620 retrievals: Operational algorithm sensitivity to particle non-sphericity, *Atmos. Meas. Tech.*, 6(8),  
621 2131–2154, doi:10.5194/amt-6-2131-2013, 2013.



622 Lamarque, J. F., Shindell, D. T., Josse, B., Young, P. J., Cionni, I., Eyring, V., Bergmann, D.,  
 623 Cameron-Smith, P., Collins, W. J., Doherty, R., Dalsoren, S., Faluvegi, G., Folberth, G., Ghan,  
 624 S. J., Horowitz, L. W., Lee, Y. H., MacKenzie, I. A., Nagashima, T., Naik, V., Plummer, D.,  
 625 Righi, M., Rumbold, S. T., Schulz, M., Skeie, R. B., Stevenson, D. S., Strode, S., Sudo, K.,  
 626 Szopa, S., Voulgarakis, A. and Zeng, G.: The atmospheric chemistry and climate model  
 627 intercomparison Project (ACCMIP): Overview and description of models, simulations and  
 628 climate diagnostics, *Geosci. Model Dev.*, 6(1), 179–206, doi:10.5194/gmd-6-179-2013, 2013.

629 Lelieveld, J., Evans, J. S., Fnais, M., Giannadaki, D. and Pozzer, A.: The contribution of outdoor  
 630 air pollution sources to premature mortality on a global scale, *Nature*, 525(7569), 367–371,  
 631 doi:10.1038/nature15371, 2015.

632 Levy, R. C., Mattoo, S., Munchak, L. A., Remer, L. A., Sayer, A. M., Patadia, F. and Hsu, N. C.:  
 633 The Collection 6 MODIS aerosol products over land and ocean, *Atmos. Meas. Tech.*, 6(11),  
 634 2989–3034, doi:10.5194/amt-6-2989-2013, 2013.

635 Liu, M., Westphal, D. L., Walker, A. L., Holt, T. R., Richardson, K. A. and Miller, S. D.:  
 636 COAMPS real-time dust storm forecasting during operation Iraqi freedom, *Weather Forecast.*,  
 637 22(1), 192–206, doi:10.1175/WAF971.1, 2007.

638 Lynch, P., Reid, J. S., Westphal, D. L., Zhang, J., Hogan, T. F., Hyer, E. J., Curtis, C. A., Hegg,  
 639 D. A., Shi, Y., Campbell, J. R., Rubin, J. I., Sessions, W. R., Turk, F. J. and Walker, A. L.: An  
 640 11-year global gridded aerosol optical thickness reanalysis (v1.0) for atmospheric and climate  
 641 sciences, *Geosci. Model Dev.*, 9(4), 1489–1522, doi:10.5194/gmd-9-1489-2016, 2016.

642 Martonchik, J. V., Kahn, R. A. and Diner, D. J.: Retrieval of aerosol properties over land using  
 643 MISR observations, in *Satellite Aerosol Remote Sensing over Land*, pp. 267–293, Springer  
 644 Berlin Heidelberg, 2009.

645 Randles, C. A., da Silva, A. M., Buchard, V., Colarco, P. R., Darmenov, A., Govindaraju, R.,  
 646 Smirnov, A., Holben, B., Ferrare, R., Hair, J., Shinozuka, Y. and Flynn, C. J.: The MERRA-2  
 647 aerosol reanalysis, 1980 onward. Part I: System description and data assimilation evaluation, *J.*  
 648 *Clim.*, 30(17), 6823–6850, doi:10.1175/JCLI-D-16-0609.1, 2017.

649 Reid, J. S., Benedetti, A., Colarco, P. R. and Hansen, J. A.: International operational aerosol  
 650 observability workshop, in Bulletin of the American Meteorological Society, vol. 92., 2011.

651 Rienecker, M. M., Suarez, M. J., Gelaro, R., Todling, R., Bacmeister, J., Liu, E., Bosilovich, M.  
 652 G., Schubert, S. D., Takacs, L., Kim, G. K., Bloom, S., Chen, J., Collins, D., Conaty, A., Da  
 653 Silva, A., Gu, W., Joiner, J., Koster, R. D., Lucchesi, R., Molod, A., Owens, T., Pawson, S.,  
 654 Pegion, P., Redder, C. R., Reichle, R., Robertson, F. R., Ruddick, A. G., Sienkiewicz, M. and  
 655 Woollen, J.: MERRA: NASA's modern-era retrospective analysis for research and applications,  
 656 J. Clim., 24, 3624–3648, doi:10.1175/JCLI-D-11-00015.1, 2011.

657 Sayer, A. M. and Knobelspiesse, K. D.: How should we aggregate data? Methods accounting for  
 658 the numerical distributions, with an assessment of aerosol optical depth, Atmos. Chem. Phys.,  
 659 19(23), 15023–15048, doi:10.5194/acp-19-15023-2019, 2019.

660 Sayer, A. M., Govaerts, Y., Kolmonen, P., Lipponen, A., Luffarelli, M., Mielonen, T., Patadia,  
 661 F., Popp, T., Povey, A. C., Stebel, K. and Witek, M. L.: A review and framework for the  
 662 evaluation of pixel-level uncertainty estimates in satellite aerosol remote sensing, Atmos. Meas.  
 663 Tech., 13(2), 373–404, doi:10.5194/amt-13-373-2020, 2020.

664 Sekiyama, T. T., Tanaka, T. Y., Shimizu, A. and Miyoshi, T.: Data assimilation of CALIPSO  
 665 aerosol observations, Atmos. Chem. Phys., 10(1), 39–49, doi:10.5194/acp-10-39-2010, 2010.

666 Shi, Y., Zhang, J., Reid, J. S., Holben, B., Hyer, E. J. and Curtis, C.: An analysis of the collection  
 667 5 MODIS over-ocean aerosol optical depth product for its implication in aerosol assimilation,  
 668 Atmos. Chem. Phys., 11(2), 557–565, doi:10.5194/acp-11-557-2011, 2011.

669 Shi, Y., Zhang, J., Reid, J. S., Hyer, E. J. and Hsu, N. C.: Critical evaluation of the MODIS Deep  
 670 Blue aerosol optical depth product for data assimilation over North Africa, Atmos. Meas. Tech.,  
 671 6(4), 949–969, doi:10.5194/amt-6-949-2013, 2013.

672 Shi, Y., Zhang, J., Reid, J. S., Liu, B. and Hyer, E. J.: Critical evaluation of cloud contamination  
 673 in the MISR aerosol products using MODIS cloud mask products, Atmos. Meas. Tech., 7(6),  
 674 1791–1801, doi:10.5194/amt-7-1791-2014, 2014.

675 Shindell, D. T., Lamarque, J. F., Schulz, M., Flanner, M., Jiao, C., Chin, M., Young, P. J., Lee,

676 Y. H., Rotstayn, L., Mahowald, N., Milly, G., Faluvegi, G., Balkanski, Y., Collins, W. J.,  
 677 Conley, A. J., Dalsoren, S., Easter, R., Ghan, S., Horowitz, L., Liu, X., Myhre, G., Nagashima,  
 678 T., Naik, V., Rumbold, S. T., Skeie, R., Sudo, K., Szopa, S., Takemura, T., Voulgarakis, A.,  
 679 Yoon, J. H. and Lo, F.: Radiative forcing in the ACCMIP historical and future climate  
 680 simulations, *Atmos. Chem. Phys.*, 13(6), 2939–2974, doi:10.5194/acp-13-2939-2013, 2013.

681 Si, Y., Chen, L., Xiong, X., Shi, S., Husi, L. and Cai, K.: Evaluation of the MISR fine resolution  
 682 aerosol product using MODIS, MISR, and ground observations over China, *Atmos. Environ.*,  
 683 223(December 2019), 117229, doi:10.1016/j.atmosenv.2019.117229, 2020.

684 Sogacheva, L., Popp, T., Sayer, A. M., Dubovik, O., Garay, M. J., Heckel, A., Hsu, N. C.,  
 685 Jethva, H., Kahn, R. A., Kolmonen, P., Kosmale, M., de Leeuw, G., Levy, R. C., Litvinov, P.,  
 686 Lyapustin, A., North, P., Torres, O. and Arola, A.: Merging regional and global aerosol optical  
 687 depth records from major available satellite products, *Atmos. Chem. Phys.*, 20(4), 2031–2056,  
 688 doi:10.5194/acp-20-2031-2020, 2020.

689 Tao, M., Wang, J., Li, R., Chen, L., Xu, X., Wang, L., Tao, J., Wang, Z. and Xiang, J.:  
 690 Characterization of Aerosol Type Over East Asia by 4.4 km MISR Product: First Insight and  
 691 General Performance, *J. Geophys. Res. Atmos.*, 125(13), 1–16, doi:10.1029/2019JD031909,  
 692 2020.

693 Di Tomaso, E., Schutgens, N. A. J., Jorba, O. and García-Pando, C. P.: Assimilation of MODIS  
 694 Dark Target and Deep Blue observations in the dust aerosol component of NMMB-MONARCH  
 695 version 1.0, *Geosci. Model Dev.*, 10(3), 1107–1129, doi:10.5194/gmd-10-1107-2017, 2017.

696 Turnock, S. T., Allen, R. J., Andrews, M., Bauer, S. E., Deushi, M., Emmons, L., Good, P.,  
 697 Horowitz, L., John, J. G., Michou, M., Nabat, P., Naik, V., Neubauer, D., O'Connor, F. M.,  
 698 Olivie, D., Oshima, N., Schulz, M., Sellar, A., Shim, S., Takemura, T., Tilmes, S., Tsigaridis, K.,  
 699 Wu, T. and Zhang, J.: Historical and future changes in air pollutants from CMIP6 models,  
 700 *Atmos. Chem. Phys.*, 20(23), 14547–14579, doi:10.5194/acp-20-14547-2020, 2020.

701 Werner, M., Kryza, M. and Guzikowski, J.: Can data assimilation of surface PM<sub>2.5</sub> and Satellite  
 702 AOD improve WRF-Chem Forecasting? A case study for two scenarios of particulate air  
 703 pollution episodes in Poland, *Remote Sens.*, 11(20), doi:10.3390/rs11202364, 2019.

704 Witek, M. L., Garay, M. J., Diner, D. J. and Smirnov, A.: Aerosol optical depths over oceans: A  
 705 view from MISR retrievals and collocated MAN and AERONET in situ observations, *J.*  
 706 *Geophys. Res. Atmos.*, 118(22), 12620–12633, doi:10.1002/2013JD020393, 2013.

707 Witek, M. L., Diner, D. J., Garay, M. J., Xu, F., Bull, M. A. and Seidel, F. C.: Improving MISR  
 708 AOD Retrievals with Low-Light-Level Corrections for Veiling Light, *IEEE Trans. Geosci.*  
 709 *Remote Sens.*, 56(3), 1251–1268, doi:10.1109/TGRS.2017.2727342, 2018a.

710 Witek, M. L., Garay, M. J., Diner, D. J., Bull, M. A. and Seidel, F. C.: New approach to the  
 711 retrieval of AOD and its uncertainty from MISR observations over dark water, *Atmos. Meas.*  
 712 *Tech.*, 11(1), 429–439, doi:10.5194/amt-11-429-2018, 2018b.

713 Witek, M. L., Garay, M. J., Diner, D. J. and Smirnov, A.: Oceanic Aerosol Loading Derived  
 714 From MISR’s 4.4 km (V23) Aerosol Product, *J. Geophys. Res. Atmos.*, 124(17–18), 10154–  
 715 10174, doi:10.1029/2019JD031065, 2019.

716 Xian, P., Reid, J. S., Hyer, E. J., Sampson, C. R., Rubin, J. I., Ades, M., Asencio, N., Basart, S.,  
 717 Benedetti, A., Bhattacharjee, P. S., Brooks, M. E., Colarco, P. R., da Silva, A. M., Eck, T. F.,  
 718 Guth, J., Jorba, O., Kouznetsov, R., Kipling, Z., Sofiev, M., Perez Garcia-Pando, C., Pradhan,  
 719 Y., Tanaka, T., Wang, J., Westphal, D. L., Yumimoto, K. and Zhang, J.: Current state of the  
 720 global operational aerosol multi-model ensemble: An update from the International Cooperative  
 721 for Aerosol Prediction (ICAP), *Q. J. R. Meteorol. Soc.*, 145, 176–209, doi:10.1002/qj.3497,  
 722 2019.

723 Zhang, J. and Reid, J. S.: An analysis of clear sky and contextual biases using an operational  
 724 over ocean MODIS aerosol product, *Geophys. Res. Lett.*, 36(15), doi:10.1029/2009GL038723,  
 725 2009.

726 Zhang, J. and Reid, J. S.: A decadal regional and global trend analysis of the aerosol optical  
 727 depth using a data-assimilation grade over-water MODIS and Level 2 MISR aerosol products,  
 728 *Atmos. Chem. Phys.*, 10(22), 10949–10963, doi:10.5194/acp-10-10949-2010, 2010.

729 Zhang, J., Reid, J. S., Westphal, D. L., Baker, N. L. and Hyer, E. J.: A system for operational  
 730 aerosol optical depth data assimilation over global oceans, *J. Geophys. Res. Atmos.*, 113(10), 1–

731 13, doi:10.1029/2007JD009065, 2008.

732